JOURNAL OF SPACECRAFT AND ROCKETS
Vol. 39, No. 1, January–February 2002

Impact Analysis of Hall Thrusters on Satellite Antenna Performance

Gary A. Hallock,[*] James C. Wiley,[†] Ashish Khanna,[‡] and Edmund A. Spencer[‡]
University of Texas at Austin, Austin, Texas 78712
and
J. William Meyer[§] and Joseph T. Loane[¶]
Lockheed Martin Space Systems Company, Sunnyvale, California 94089

A geometrical optics ray-tracing code has been developed to study the effect of plasma thrusters on communication satellite antennas. This code has flexible three-dimensional geometry and a friendly web-based interface. A study is reported where a thruster is directed perpendicular to a 1-m reflector antenna 0.5 m away. The thruster is translated away from the reflector, and the main lobe attenuation, H-plane main lobe full width, and cross polarization are analyzed at 0.2-m increments. These studies are done at 5 and 10 GHz.

Nomenclature

A = ideal parabolic reflector electric field, Vm^{-1}
A_{ref} = reference electric field, Vm^{-1}
A_θ, A_ϕ = unnormalized pattern electric field, Vm^{-1}
$\mathcal{A}$ = ray tube area, m^2
a = effective ray tube radius, m
a_1 = density fit parameter, m^{-1}
$\hat{\boldsymbol{b}}$ = ray binormal unit vector
C = edge taper parameter
DF = divergence factor
E_t = edge taper, dB
$\boldsymbol{E}_A$ = exit plane electric field, Vm^{-1}
E_0 = initial ray electric field intensity, Vm^{-1}
e = elementary charge, C
$\boldsymbol{H}_A$ = exit plane magnetic intensity, Am^{-1}
$\mathcal{I}$ = optical path length, m
k_0 = signal free-space wave number
m_e = electron mass, kg
N = plasma refractive index
$\hat{\boldsymbol{n}}$ = ray normal unit vector
n_e = electron density, m^{-3}
p = aperture profile parameter and power density, Wm^{-2}
R = reflector radius, m
S = ray tube shape factor
s = arclength along ray trajectory, m
$\hat{\boldsymbol{t}}$ = ray tangent unit vector
α = density fit parameter, deg^{-1}
ϵ_0 = permittivity of free space, Fm^{-1}
η = impedance of free space, Ω
θ = integrated torsion
κ = ray or wavefront curvature, $1/\rho$, m^{-1}
κ_u, κ_v = principal wavefront curvatures, m^{-1}
ρ = ray or wavefront radius of curvature, $1/\kappa$, m
τ = ray torsion, m^{-1}
ϕ = ray phase shift and spherical coordinate angle
ϕ_0 = vacuum ray phase shift and spherical coordinate angles 0, $\pi/2$
ω = signal frequency, s^{-1}
ω_p = plasma frequency, s^{-1}

Introduction

HALL thrusters are currently under development for stationkeeping of geosynchronous communications satellites. These thrusters produce an inhomogeneous plasma plume, which must be carefully evaluated in terms of possibe degradation of the microwave communications signals. Such plume effects include pointing error and attenuation of the main antenna lobe, side lobe changes, and induced cross polarization.

This interaction has been investigated by several groups,[1–3] and detailed plume modeling is underway.[4] In this paper a code using a combination of geometrical optics (GO) ray tracing and aperture field integration to analyze the effects of plasma thrusters on antenna performance is reported. This approach allows realistic three-dimensional geometries to be studied in detail. Several parametric scans are presented that indicate how the plume–antenna interaction changes as the configuation is varied. This work quantitatively identifies changes in the antenna pattern, which is of value to the systems designer.

One general tendency of the plasma refraction is to squint the beam away from the plume. This will shift the edge-of-coverage contour of the far-field antenna pattern on Earth. Because the gain slope with respect to pointing angle is relatively steep near the edge of coverage, this can impact receivers on one side of the served customer area by loss of signal strength. Furthermore, thruster plumes are unstable, showing up to 100% density fluctuations in the tens of kilohertz. The signal strength at the edge of coverage will jitter in accordance with this modulation.[5] Therefore, it is necessary to locate the thruster and antenna so that the signal degradation induced by the plume is below acceptable limits. A rigorous calculation is required to predict small changes in the antenna pattern with high confidence.

There is interest in plume effects over a wide range of signal frequencies, approximately 1–20 GHz. Numerical specifications for the level of degradation that can be tolerated will depend on the payload. A typical system-level beam pointing accuracy requirement might be 0.15 deg, which can be converted to an edge-of-coverage gain loss. However, it would not be acceptable to apportion more than a fraction of the 0.15 deg to thruster effects. One would generally like the code to be able to predict beam-pointing error to about a hundredth of a beamwidth.

In addition to the beam-distortion issue, other areas of concern are polarization purity, side lobe levels, polarization isolation, and

---

Presented as Paper 2000-3519 at the AIAA/ASME/SAE/ASEE 36th Joint Propulsion Conference, Huntsville, AL, 16–19 July 2000; received 27 February 2001; revision received 8 September 2001; accepted for publication 10 September 2001.

[*] Professor, Electrical and Computer Engineering Department. Member AIAA.

[†] Research Scientist, Fusion Research Center. Member AIAA.

[‡] Graduate Research Assistant, Electrical and Computer Engineering Department.

[§] Technical Fellow, Design Engineering. Member AIAA.

[¶] Research Specialist, Advanced Telecommunications Technology.

phase (or amplitude) modulation. Phase modulation introduces sidebands in the signal spectrum at frequency multiples of the thruster oscillations. The code covered in this paper addresses all of these areas with the exception of the modulation problem.

The ray-tracing code launches a set of rays from a plane (antenna aperture) and tracks the rays until they impinge on a specified mathematical surface, called the exit plane. The code computes the amplitude, trajectory, phase, and polarization of each ray, based on the laws of GO. The exit plane is located sufficiently far away so that it is essentially located in free space, that is, the plasma density has dropped to approximately zero. Once the electric field on the exit plane has been determined, the far-field radiation pattern is obtained from the radiation integral, derived from Huygen's principle. This work is based on our previous analysis of arcjet thrusters.[6]

An electrically large volume problem as exists here is most practically handled with optical methods such as GO. At the lowest frequencies, it would be possible to run an electromagnetic finite element code, at least on the plume part of the problem. However, because this would require much more computation time with no guarantee of improved accuracy, and would not provide as much insight, this approach is not taken. Commercial ray-tracing codes are generally designed for optical applications with material media and do not easily offer the flexibility of the code reported here.

Hall Thruster

The electron density on the axis of a 5-kW class Hall thruster (HT) at a distance of 1 m is on the order of 10^{16} m^{-3}. This density decreases with distance along the axis as approximately $1/r^2$. Offaxis, there is a gradual density decrease with angle that leaves the thruster plume fairly broad. Most of the electrons are contained within a cone of 45-deg half angle, but there are some well beyond this.

The plasma frequency is defined as

$$\omega_p = \sqrt{n_e e^2 \big/ \epsilon_0 m_e} \tag{1}$$

that is, ω_p^2 is proportional to n_e. The 10^{16}-m^{-3} electron number density corresponds to a plasma frequency of 0.9 GHz. Signals at and below the plasma frequency cannot propagate through this density of plasma. Frequencies higher than ω_p will propagate without attenuation, because the plasma is well approximated as collisionless. However, microwaves propagating through the plasma exhibit a phase shift relative to vacuum and refraction by the medium. For a satellite antenna and an HT mounted near each other, this can distort the antenna pattern.

The plasma refractive index

$$N = \sqrt{\epsilon/\epsilon_0} = \sqrt{1 - \omega_p^2 \big/ \omega^2} \tag{2}$$

is a function of n_e/ω^2, where we assume the plasma is cold, unmagnetized, and collisionless. These conditions are well satisfied in the plume of an HT in geosynchronous orbit. The overall effect in terms of index of refraction and phase shift drops off with signal frequency ω. In low-density parts of the plume, the total phase shift is proportional to n_e/ω times the path length.

There can be significant refraction and phase shift even when the frequency is far higher than the cutoff condition given by $\omega = \omega_p$. Except for very high-frequency systems, signal paths through the high-density regions of the plume must be avoided. Figure 1 gives approximate calculations of the phase shift relative to vacuum along straight grid lines through a representative 5-kW class HT plume

$$\phi_0 - \phi = k_0 \int (1 - N)\, \mathrm{d}s \tag{3}$$

The physical path lengths are from a parallel plane 8 m on one side of the plume axis to 8 m on the other side, which captures most of the plasma. Results are included for 1, 5, and 10 GHz (L, C, and X bands). This is a scalar nonbending ray calculation and so it is only an approximate indication of the phase shift of an actual signal. Although precise judgements cannot be made from these simple calculations, they show the integrated effect and illustrate the much reduced size of the refractive HT plume at higher signal frequencies. Satellite thruster mounting options should take this into account.

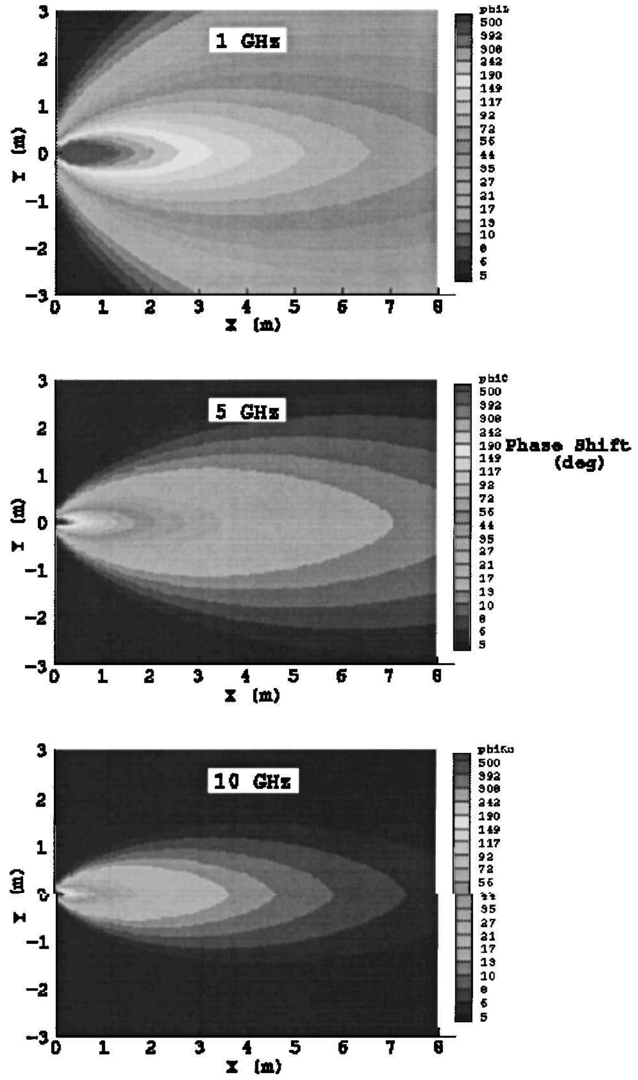

Fig. 1 Cross-plume scalar phase shift maps for a 5-kW class Hall thruster.

To model the plume density in the code, it is assumed that the plume expansion in the far flowfield is dominated by gasdynamic expansion, at relatively constant electron velocity. The plasma density may then be treated as though it originates from a point source. We use the functional form

$$n_e = \left(a_1 \big/ r^2\right) e^{-\alpha\theta} \text{ m}^{-3} \tag{4}$$

where r is the distance from the thruster nozzle and θ is the angle from the thruster axis, which provided a good fit to experimental arcjet measurements.[7,8] More recently, Ohler et al.[9] have used this expression in modeling the far field of an HT, obtaining good agreement with experimental plume measurements. Parameters a_1 and α are adjusted to give the best fit to the available thruster data.

Ray-Tracing Code

The ray-tracing code, BeamServer, is written in C++. It is a major extension of earlier work coded in FORTRAN.[10] Changes to the original codes include a variable step size differential equation solver (rather than finite differencing), computation of the plasma density gradient directly from the plasma density function (rather than requiring an analytic expression), improved divergence factor calculations, object-oriented programming (allowing fully flexible three-dimensional geometry, multiple thrusters, and simpler upgrades), and a web-based interface.

Ray Trajectories

The trajectory of a ray in space is described by its position vector $\boldsymbol{r}$ and three orthogonal unit vectors, as shown in Fig. 2. Defining s

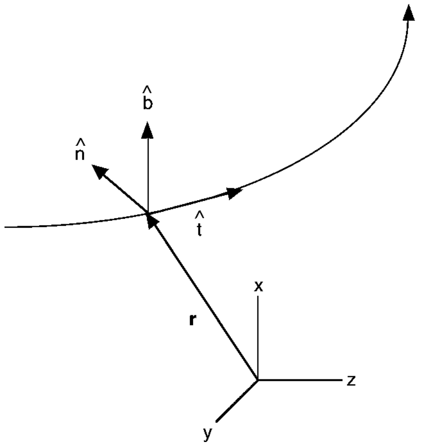

Fig. 2 Ray trajectory vectors.

as the arclength along the curved ray trajectory, the tangent, normal, and binormal vectors are defined by

$$\hat{\boldsymbol{t}} = \frac{\mathrm{d}\boldsymbol{r}}{\mathrm{d}s} = \boldsymbol{r}' \tag{5}$$

$$\hat{\boldsymbol{n}} = \frac{1}{\kappa}\frac{\mathrm{d}\hat{\boldsymbol{t}}}{\mathrm{d}s} = \rho\hat{\boldsymbol{t}}' \tag{6}$$

$$\hat{\boldsymbol{b}} = \hat{\boldsymbol{t}} \times \hat{\boldsymbol{n}} \tag{7}$$

respectively, where the rate of change of the tangent vector $\hat{\boldsymbol{t}}$ is the ray curvature $\kappa = |\hat{\boldsymbol{t}}'|$ and $\rho = 1/\kappa$ is the radius of curvature.

The rate of change of the binormal vector $\hat{\boldsymbol{b}}$ is known as the torsion[11] τ:

$$\frac{\mathrm{d}\hat{\boldsymbol{b}}}{\mathrm{d}s} = \hat{\boldsymbol{b}}' = -\tau\hat{\boldsymbol{n}} \tag{8}$$

The torsion measures the turning of the binormal vector. The integral of the torsion along the ray gives the rotation of the wave polarization vector in the local $\hat{\boldsymbol{n}}, \hat{\boldsymbol{b}}$ coordinate system,

$$\theta = \int \tau \, \mathrm{d}s \tag{9}$$

The code advances the ray a distance ds by calling an ordinary differential equation (ODE) solver routine. Here we are using a Bulirsch–Stoer algorithm (see Ref. 12). An ODE solver is typically constructed to solve a system of coupled equations of the form

$$\frac{\mathrm{d}\boldsymbol{y}}{\mathrm{d}t} = \boldsymbol{f}(\boldsymbol{y}) \tag{10}$$

where the function $\boldsymbol{f}$ is supplied by an auxiliary routine. Here the four equations for the position $\boldsymbol{r}$, tangent vector $\hat{\boldsymbol{t}}$, optical length $\mathcal{I}$, and polarization angle θ

$$\frac{\mathrm{d}\boldsymbol{r}}{\mathrm{d}s} = \hat{\boldsymbol{t}} \tag{11}$$

$$\frac{\mathrm{d}\hat{\boldsymbol{t}}}{\mathrm{d}s} = \kappa\hat{\boldsymbol{n}} \tag{12}$$

$$\frac{\mathrm{d}\mathcal{I}}{\mathrm{d}s} = N \tag{13}$$

$$\frac{\mathrm{d}\theta}{\mathrm{d}s} = \tau \tag{14}$$

are integrated.

Once the ODE solver has computed the new position, tangent vector, optical path length, and integrated torsion of a ray, the new unit normal vector and curvature are found from the fundamental equation of GO

$$\kappa\hat{\boldsymbol{n}} = \frac{\mathrm{d}\hat{\boldsymbol{t}}}{\mathrm{d}s} = \frac{\nabla N}{N} - \frac{1}{N}(\nabla N \cdot \hat{\boldsymbol{t}})\hat{\boldsymbol{t}} \tag{15}$$

The new binormal unit vector is then

$$\hat{\boldsymbol{b}} = \hat{\boldsymbol{t}} \times \hat{\boldsymbol{n}} \tag{16}$$

The new torsion can then be found from

$$\tau = \frac{1}{\kappa N}\frac{\mathrm{d}\nabla N}{\mathrm{d}s} \cdot \hat{\boldsymbol{b}} \tag{17}$$

The index of refraction is assumed to have at least second derivitives so that $(\nabla N)'$ can be calculated from

$$\frac{\mathrm{d}\nabla N}{\mathrm{d}s} = \begin{pmatrix} \dfrac{\partial^2 N}{\partial x^2}t_x + \dfrac{\partial^2 N}{\partial x \partial y}t_y + \dfrac{\partial^2 N}{\partial x \partial z}t_z \\[2ex] \dfrac{\partial^2 N}{\partial y \partial x}t_x + \dfrac{\partial^2 N}{\partial y^2}t_y + \dfrac{\partial^2 N}{\partial y \partial z}t_z \\[2ex] \dfrac{\partial^2 N}{\partial z \partial x}t_x + \dfrac{\partial^2 N}{\partial z \partial y}t_y + \dfrac{\partial^2 N}{\partial z^2}t_z \end{pmatrix} \tag{18}$$

The index of refraction N integrated along the ray path is known as the optical length $\mathcal{I}$ and is related to the wave phase change ϕ along a ray by

$$\phi = k_0 \int N \, \mathrm{d}s = k_0 \mathcal{I} \tag{19}$$

where k_0 is the free-space wave number.

Divergence Factor

If one considers a differential ray tube rather than a single ray, its cross-sectional area will change as it travels through space if the medium is inhomogeneous. Conservation of energy along a ray tube requires

$$p_1(\mathrm{d}A_1) = p_2(\mathrm{d}A_2) \tag{20}$$

where $p = E^2/2\eta$ W/m^2. The subscripts indicate two locations along a ray tube, as shown in Fig. 3. This gives the electric field magnitude

$$E_2 = \mathrm{DF}\sqrt{N_1/N_2}E_1 \tag{21}$$

where DF is defined at point 2 relative to point 1 along a ray by

$$\mathrm{DF} = \sqrt{\frac{\mathrm{d}A_1}{\mathrm{d}A_2}} \tag{22}$$

The dAs give the cross-sectional area of the differential ray tube, as shown in Fig. 3. In addition, the DF is made a complex quantity and used to keep track of the $\exp(i\pi/2)$ phase jumps that occur when a ray passes through a focus.[13]

As shown by Bremmer and Lee [Eq. (25b) of Ref. 13], the DF is also given by

$$\mathrm{DF} = \exp\left[-\frac{1}{2}\int_{s_1}^{s_2} (\kappa_u + \kappa_v) \, \mathrm{d}s\right] \tag{23}$$

where κ_u and κ_v are the principal curvatures of the wavefront surface.

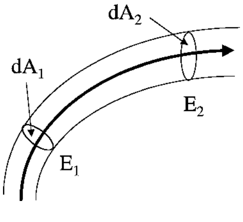

Fig. 3 Cross-sectional area of a ray tube.

The principal curvatures κ_u and κ_v are calculated by integrating two additional rays slightly displaced from the main ray for the same optical length. The three rays then provide three points on the same wavefront. From these three points, the required curvatures are obtained, as discussed in the following section. Near a focus, a different procedure is followed. In this case, four paraxial rays are generated, and Eq. (22) is used directly, that is, the change in cross-sectional area of the ray tube is computed on each side of the focus. The phase jump is also included.

Wavefront Calculation

At the end of each integration step, two side rays have also been integrated to have the same optical path as the central ray. The endpoints of the three rays, $\boldsymbol{P}_0$ (central ray), $\boldsymbol{P}_1$ and $\boldsymbol{P}_2$ (side rays) are all on the same wavefront and not collinear by construction. These points are used to estimate the principal directions on the wavefront surface and the curvature of the wavefront in these two directions.

Let $\mathrm{d}\boldsymbol{r}$ be a tangent vector on the wavefront surface and let $\hat{\boldsymbol{t}}$ be a unit vector normal to the surface (tangent to a ray). The ray tangent vectors at the three points are known from the integration, so that the surface normals at those points are also known. The curvature of the surface can be expressed as

$$\kappa = \frac{\mathrm{d}\boldsymbol{r} \cdot \mathrm{d}\hat{\boldsymbol{t}}}{\mathrm{d}\boldsymbol{r} \cdot \mathrm{d}\boldsymbol{r}} \tag{24}$$

Define two directions in the surface from $\boldsymbol{P}_0$, $\hat{\boldsymbol{u}}$ and $\hat{\boldsymbol{v}}$, by the unit vectors

$$\hat{\boldsymbol{u}} = \frac{\boldsymbol{P}_1 - \boldsymbol{P}_0}{|\boldsymbol{P}_1 - \boldsymbol{P}_0|} \tag{25}$$

$$\hat{\boldsymbol{v}} = \frac{\boldsymbol{P}_2 - \boldsymbol{P}_0}{|\boldsymbol{P}_2 - \boldsymbol{P}_0|} \tag{26}$$

as shown in Fig. 4.

In the region of $\boldsymbol{P}_0$, $\mathrm{d}\boldsymbol{r}$ can be given by

$$\mathrm{d}\boldsymbol{r} = \boldsymbol{P}(t_1, t_2) - \boldsymbol{P}_0 = \frac{(\boldsymbol{P}_1 - \boldsymbol{P}_0)}{|\boldsymbol{P}_1 - \boldsymbol{P}_0|}t_1 + \frac{(\boldsymbol{P}_2 - \boldsymbol{P}_0)}{|\boldsymbol{P}_2 - \boldsymbol{P}_0|}t_2 = t_1\hat{\boldsymbol{u}} + t_2\hat{\boldsymbol{v}} \tag{27}$$

where t_1 and t_2 parameterize $\mathrm{d}\boldsymbol{r}$ in the $\hat{\boldsymbol{u}}$ and $\hat{\boldsymbol{v}}$ directions, respectively. Also, the normal to the surface in this region is given by

$$\mathrm{d}\hat{\boldsymbol{t}} = \hat{\boldsymbol{t}} - \hat{\boldsymbol{t}}_0 = \frac{(\hat{\boldsymbol{t}}_1 - \hat{\boldsymbol{t}}_0)}{|\boldsymbol{P}_1 - \boldsymbol{P}_0|}t_1 + \frac{(\hat{\boldsymbol{t}}_2 - \hat{\boldsymbol{t}}_0)}{|\boldsymbol{P}_2 - \boldsymbol{P}_0|}t_2 = t_1\boldsymbol{t}_u + t_2\boldsymbol{t}_v \tag{28}$$

where t_1 and t_2 parameterize $\mathrm{d}\hat{\boldsymbol{t}}$ and

$$\boldsymbol{t}_u = \frac{(\hat{\boldsymbol{t}}_1 - \hat{\boldsymbol{t}}_0)}{|\boldsymbol{P}_1 - \boldsymbol{P}_0|} \tag{29}$$

$$\boldsymbol{t}_v = \frac{(\hat{\boldsymbol{t}}_2 - \hat{\boldsymbol{t}}_0)}{|\boldsymbol{P}_2 - \boldsymbol{P}_0|} \tag{30}$$

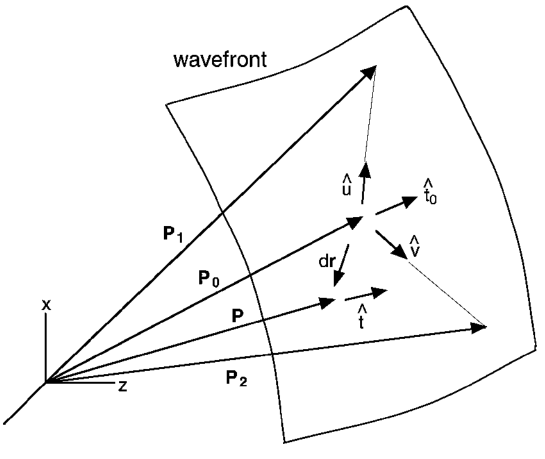

Fig. 4 Vectors used to calculate the principal curvatures of wavefront.

Substituting into the expression for κ, we have

$$\kappa = \frac{t_1^2\hat{\boldsymbol{u}} \cdot \boldsymbol{t}_u + t_1t_2(\hat{\boldsymbol{u}} \cdot \boldsymbol{t}_v + \hat{\boldsymbol{v}} \cdot \boldsymbol{t}_u) + t_2^2\hat{\boldsymbol{v}} \cdot \boldsymbol{t}_v}{t_1^2\hat{\boldsymbol{u}} \cdot \hat{\boldsymbol{u}} + 2t_2t_1\hat{\boldsymbol{u}} \cdot \hat{\boldsymbol{v}} + t_2^2\hat{\boldsymbol{v}} \cdot \hat{\boldsymbol{v}}} \tag{31}$$

We define

$$E = \hat{\boldsymbol{u}} \cdot \hat{\boldsymbol{u}} = 1 \tag{32}$$

$$F = \hat{\boldsymbol{u}} \cdot \hat{\boldsymbol{v}} = \frac{(\boldsymbol{P}_1 - \boldsymbol{P}_0) \cdot (\boldsymbol{P}_2 - \boldsymbol{P}_0)}{|\boldsymbol{P}_1 - \boldsymbol{P}_0||\boldsymbol{P}_2 - \boldsymbol{P}_0|} \tag{33}$$

$$G = \hat{\boldsymbol{v}} \cdot \hat{\boldsymbol{v}} = 1 \tag{34}$$

$$e = \hat{\boldsymbol{u}} \cdot \boldsymbol{t}_u \tag{35}$$

$$g = \hat{\boldsymbol{v}} \cdot \boldsymbol{t}_v \tag{36}$$

$$f = \tfrac{1}{2}(\hat{\boldsymbol{u}} \cdot \boldsymbol{t}_v + \hat{\boldsymbol{v}} \cdot \boldsymbol{t}_u) \tag{37}$$

so that κ becomes

$$\kappa(t_1, t_2) = \frac{et_1^2 + 2ft_1t_2 + gt_2^2}{Et_1^2 + 2Ft_1t_2 + Gt_2^2} \tag{38}$$

where the denominator may be recognized as the first fundamental form and represents the arc length $\mathrm{d}s^2$ (Ref. 14). The curvature varies with t_1 and t_2. The maximum and minimum values of the curvature are the principal curvatures with the associated principal directions.[11]

The extreme values can be found by setting the first derivatives to zero:

$$\frac{\partial\kappa}{\partial t_1} = 0 = \left[\frac{2}{Et_1^2 + 2Ft_1t_2 + Gt_2^2}\right][(e - \kappa E)t_1 + (f - \kappa F)t_2] \tag{39}$$

$$\frac{\partial\kappa}{\partial t_2} = 0 = \left[\frac{2}{Et_1^2 + 2Ft_1t_2 + Gt_2^2}\right][(f - \kappa F)t_1 + (g - \kappa G)t_2] \tag{40}$$

This is a singular linear system of equations for t_1 and t_2. For the system to have a nontrivial solution, the determinant

$$\begin{vmatrix} (e - \kappa E) & (f - \kappa F) \\ (f - \kappa F) & (g - \kappa G) \end{vmatrix} \tag{41}$$

must vanish. Setting the determinant to zero produces the characteristic equation

$$(EG - F^2)\kappa^2 - (gE + eG - 2Ff)\kappa + (eg - f^2) = 0 \tag{42}$$

By defining

$$A = \frac{gE + eG - 2fF}{EG - F^2} = \frac{g + e - 2fF}{2(1 - F^2)} \tag{43}$$

$$B = \frac{eg - f^2}{EG - F^2} = \frac{eg - f^2}{1 - F^2} \tag{44}$$

we have the quadratic equation

$$\kappa^2 - 2\kappa A + B = 0 \tag{45}$$

Note that the divisions in Eqs. (43) and (44) are safe because $\hat{\boldsymbol{u}} \cdot \hat{\boldsymbol{v}} < 1$ for $\hat{\boldsymbol{u}}$ not parallel to $\hat{\boldsymbol{v}}$. The quadratic can be solved using the formulation in Ref. 12:

$$q = A + \mathrm{sgn}(A)\sqrt{A^2 - B} \tag{46}$$

$$\kappa_1 = q = \kappa_u \tag{47}$$

$$\kappa_2 = B/q = \kappa_v \tag{48}$$

giving the principal curvatures of the wavefront.

Returning to the linear system to find t_1 and t_2, we have

$$(e-\kappa_{1,2})t_1+(f-\kappa_{1,2}F)t_2=0 \tag{49}$$

Defining

$$\lambda=t_2/t_1 \tag{50}$$

for $(f-\kappa_{1,2}F)\neq 0$, we have

$$\lambda_{1,2}=\frac{\kappa_{1,2}-e}{f-\kappa_{1,2}F} \tag{51}$$

The principal directions are then

$$\hat{\boldsymbol{p}}_{1,2}=\frac{\hat{\boldsymbol{u}}+\lambda_{1,2}\hat{\boldsymbol{v}}}{\left(1+2F\lambda_{1,2}+\lambda_{1,2}^2\right)^{\frac{1}{2}}} \tag{52}$$

For the case where $(f-\kappa_{1,2}F)=0$, either because $f=0$ and $F=0$ or because $\kappa=f/F$, we have

$$\kappa=(e+g\lambda^2)/(1+\lambda^2) \tag{53}$$

which has extrema when $\lambda\to 0$ and $\lambda\to\infty$. The resulting principal directions are $\hat{\boldsymbol{u}}$ and $\hat{\boldsymbol{v}}$ with κ equal to e and g, respectively.

If $\kappa_1=\kappa_2$, Eq. (52) only gives one direction, and the curvature is the same in both directions. This represents a ray tube with a spherical wavefront. In this case, the second principal direction is choosen to be perpendicular to $\hat{\boldsymbol{t}}$ and the first principal direction.

Aperture Feed Model

Each ray is launched from a planar rectangular grid in a direction normal to the grid. The grid spacing is set by the aperture (reflector) size and the number of rays specified. The initial area of each ray is set to the grid size. The initial electric field across the aperture is given by

$$E_0(r)=C+(1-C)[1-(r/R)^2]^p \tag{54}$$

were C and p are profile parameters[15] and R is the reflector radius. The edge taper E_t (ratio of the field intensity at the reflector center to the intensity at its edge in decibels) is related to C by

$$E_t=-20\log C \tag{55}$$

The value of p is set to two. Note that the electric field at $r=0$ is unity. Rays are only launched for $r<R$.

Exit Plane

The ray calculation supplies the point of intersection of a ray with the exit plane $\boldsymbol{P}_r$ and other parameters associated with a ray. The electric field at the exit plane is then calculated from

$$\boldsymbol{E}_A=E_0e^{-ik_0\mathcal{I}}\mathrm{DF}\sqrt{N_i/N_f}\hat{\boldsymbol{e}}_f \tag{56}$$

where N_i is the initial index of refraction, N_f is the final index of refraction, and $\hat{\boldsymbol{e}}_f$ is the final polarization vector calculated from[16]

$$\hat{\boldsymbol{e}}_f=\hat{\boldsymbol{n}}_f\cos(\theta_i-\theta_f)+\hat{\boldsymbol{b}}_f\sin(\theta_i-\theta_f) \tag{57}$$

where $\hat{\boldsymbol{n}}_f$ and $\hat{\boldsymbol{b}}_f$ are the final trihedral vectors and θ_f is the final polarization rotation angle (integrated torsion). The initial polarization angle θ_i is defined by the initial polarization vector and the initial directions of $\hat{\boldsymbol{n}}$ and $\hat{\boldsymbol{b}}$,

$$\theta_i=\tan^{-1}(\beta_i/\alpha_i) \tag{58}$$

with the initial polarization vector $\boldsymbol{e}_i$,

$$\boldsymbol{e}_i=\alpha_i\hat{\boldsymbol{n}}_i+\beta_i\hat{\boldsymbol{b}}_i \tag{59}$$

Pattern Calculation

The far-field antenna pattern is computed from the field on the exit aperture. The elemental contribution from each ray is integrated (summed) using an approximation to the radiation integral derived from Huygen's principle. If $\boldsymbol{E}(\boldsymbol{r})=\boldsymbol{E}(r,\theta,\phi)$ is the electric field at a far-field observation point $\boldsymbol{r}=r\hat{\boldsymbol{r}}$, then

$$\boldsymbol{E}(r,\theta,\phi)=(e^{-ik_0r}/r)(A_\theta\hat{\boldsymbol{\theta}}+A_\phi\hat{\boldsymbol{\phi}}) \tag{60}$$

where $k_0r\to\infty$. A_θ and A_ϕ may be obtained by integrating over the wavefront of the ray tube (formulation I)[17] or by integrating over the projection of the ray tube on the exit plane (formulation II).[18] Formulation I is given by

$$\begin{bmatrix}A_\theta\\A_\phi\end{bmatrix}=\frac{ik_0}{2\pi}\iint e^{ik_0\hat{r}\cdot r'}\frac{1}{2}\left\{\begin{bmatrix}-\hat{\boldsymbol{\phi}}\\\hat{\boldsymbol{\theta}}\end{bmatrix}\times\boldsymbol{E}_A(\boldsymbol{r}')+\eta\begin{bmatrix}\hat{\boldsymbol{\theta}}\\\hat{\boldsymbol{\phi}}\end{bmatrix}\times\boldsymbol{H}_A(\boldsymbol{r}')\right\}\cdot\hat{\boldsymbol{t}}\,\mathrm{d}x'\,\mathrm{d}y' \tag{61}$$

where the integration is over the exit ray tube cross section, η is the impedance of free space, and $\hat{\boldsymbol{t}}$ is the ray tube tangent vector. Formulation II is given by

$$\begin{bmatrix}A_\theta\\A_\phi\end{bmatrix}=\frac{ik_0}{2\pi}\iint e^{ik_0\hat{r}\cdot r'}\frac{1}{2}\left\{\begin{bmatrix}-\hat{\boldsymbol{\phi}}\\\hat{\boldsymbol{\theta}}\end{bmatrix}\times\boldsymbol{E}_A(\boldsymbol{r}')+\eta\begin{bmatrix}\hat{\boldsymbol{\theta}}\\\hat{\boldsymbol{\phi}}\end{bmatrix}\times\boldsymbol{H}_A(\boldsymbol{r}')\right\}\cdot\hat{\boldsymbol{u}}\,\mathrm{d}v\,\mathrm{d}w \tag{62}$$

where the integration is over the exit ray tube projection on the exit plane and $\hat{\boldsymbol{u}}$ is a unit vector normal to the exit plane. These two formulations give similar results.

The total field components are obtained from Eq. (61) or Eq. (62) by summing the contributions from each ray. For j rays

$$A_\theta=\frac{1}{2}\frac{ik_0}{2\pi}\sum_j(B_\theta T)_j \tag{63}$$

$$A_\phi=\frac{1}{2}\frac{ik_0}{2\pi}\sum_j(B_\phi T)_j \tag{64}$$

where for formulation I

$$B_\theta=[\boldsymbol{E}_A\times\hat{\boldsymbol{\phi}}-(\boldsymbol{H}_A\times\hat{\boldsymbol{\theta}})\eta]\cdot\hat{\boldsymbol{t}} \tag{65}$$

$$B_\phi=[-\boldsymbol{E}_A\times\hat{\boldsymbol{\theta}}-(\boldsymbol{H}_A\times\hat{\boldsymbol{\phi}})\eta]\cdot\hat{\boldsymbol{t}} \tag{66}$$

or for formulation II

$$B_\theta=[\boldsymbol{E}_A\times\hat{\boldsymbol{\phi}}-(\boldsymbol{H}_A\times\hat{\boldsymbol{\theta}})\eta]\cdot\hat{\boldsymbol{u}} \tag{67}$$

$$B_\phi=[-\boldsymbol{E}_A\times\hat{\boldsymbol{\theta}}-(\boldsymbol{H}_A\times\hat{\boldsymbol{\phi}})\eta]\cdot\hat{\boldsymbol{u}} \tag{68}$$

$$T=\mathcal{A}_{\mathrm{eff}}e^{ik_0\hat{r}\cdot P_A}S(u) \tag{69}$$

The final area of the ray tube, $\mathcal{A}_f$, is given by

$$\mathcal{A}_f=\pi a^2=\mathcal{A}_i\big/|\mathrm{DF}|^2 \tag{70}$$

where $\mathcal{A}_i$ is the initial ray tube area. $\mathcal{A}_{\mathrm{eff}}$ is the effective area given by

$$\mathcal{A}_{\mathrm{eff}}=\mathcal{A}_f \tag{71}$$

for formulation I and

$$\mathcal{A}_{\mathrm{eff}}=\mathcal{A}_f/\hat{\boldsymbol{t}}\cdot\hat{\boldsymbol{u}} \tag{72}$$

for formulation II. In Eq. (69), $\boldsymbol{P}_A$ is the position vector that locates the intersection of the ray with the exit plane.

The shape factor $S(u)$

$$S(u) = 2J_1(u)/u \tag{73}$$

where J_1 is the first-order Bessel function, approximates the integral

$$S(\theta,\phi) = \frac{1}{\mathcal{A}_{\text{eff}}}\iint e^{ik_0\hat{r}\cdot r_B}\,\mathrm{d}x\,\mathrm{d}y \tag{74}$$

where $\boldsymbol{r}_B$ is the distance from the tube axis to the integration point (x, y) in the projection formulation. For formulation I, u is

$$u = k_0 a\sqrt{1-(\hat{\boldsymbol{r}}\cdot\hat{\boldsymbol{t}})^2} \tag{75}$$

whereas for formulation II

$$u = k_0 a\sqrt{[(\hat{\boldsymbol{r}}-\hat{\boldsymbol{t}})\cdot\hat{\boldsymbol{v}}]^2 + [(\hat{\boldsymbol{r}}-\hat{\boldsymbol{t}})\cdot\hat{\boldsymbol{w}}]^2} \tag{76}$$

Normalization

The antenna pattern is normalized relative to an ideal parabolic reflector with radius R and an amplitude distribution across the aperture given by Eq. (54). For the case with no central blockage and $p = 2$, the amplitude in the far field at $\theta = 0$ is

$$A_{\text{ref}} = (ik_0/2\pi)(\pi R^2)\left[C + \tfrac{1}{3}(1-C)\right] \tag{77}$$

which is used to normalize the results.

The code calculates and displays

$$E_{\theta n}(\theta,\phi_0) = |A_\theta(\theta,\phi_0)/A_{\text{ref}}| \tag{78}$$

$$E_{\phi n}(\theta,\phi_0) = |A_\phi(\theta,\phi_0)/A_{\text{ref}}| \tag{79}$$

for $\phi_0 = 0, \pi/2$. Usually the initial ray polarizations are set so that $\phi_0 = 0, \pi/2$ represent the H-plane and the E-plane antenna patterns.

Reference Pattern

With no central blockage ($R_0 = 0$), the far-field integral expression for an ideal parabolic reflector[15]

$$A = \frac{ik_0}{2\pi}\int_{R_0}^{R}\int_0^{2\pi} E_0(r')\exp[ik_0 r'\sin(\theta)\cos(\phi - \phi')]r'\mathrm{d}r'\mathrm{d}\phi' \tag{80}$$

can be integrated in closed form to give

$$A = (ik_0/2\pi)(\pi R^2)[C\Lambda_1(u) + (1-C)\Lambda_{p+1}(u)] \tag{81}$$

where

$$\Lambda_{p+1}(u) = 2^{p+1}\Gamma(p+1)\left[J_{p+1}(u)\big/u^{p+1}\right] \tag{82}$$

and $u = kR\sin\theta$. For $p = 2$ and $\theta = 0$, Eq. (77) is obtained. Equation (81) can be plotted with the ray-tracing results to observe changes from this free-space reference pattern.

Results

To study the effect of an HT on the performance of a reflector antenna, we consider the configuration shown in Fig. 5. A 1-m-diam parabolic reflector is located at the origin of the code coordinate system in the xy plane. Rays are launched in the z direction, to an exit plane at $z = 1$ m. The initial polarization is in the y direction. In the H-plane, E_ϕ is the copolarized field and E_θ the cross-polarized field. In the E-plane, E_θ is the copolarized field and E_ϕ the cross-polarized field. The thruster nozzle is located 0.5 m from the reflector ($x = x_p$, $y = 0$, and $z = 0.5$ m). The thruster is directed along x, and x_p is changed for various code runs.

Two frequencies are studied, 5 and 10 GHz. Rays are launched from the reflector plane with $\lambda/4$ separation in x and y (1.5 cm for 5-GHz cases and 0.75 cm for 10-GHz cases), to well exceed Nyquist sampling. A 10-dB edge taper is used. The thruster parameters are $a_1 = 2\times10^{16}$ m^{-1} and $\alpha = 0.07$ deg^{-1}. For these frequencies and the geometry of this configuration, the interaction is well approximated using the far fields of both the antenna and thruster.

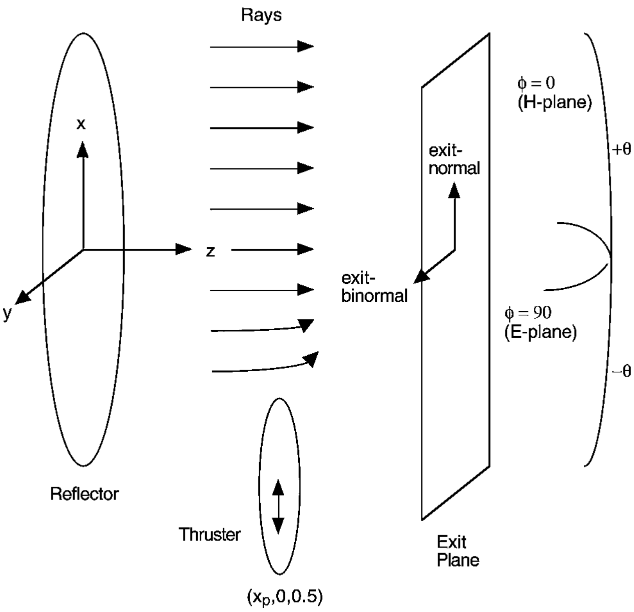

Fig. 5 Configuration studied.

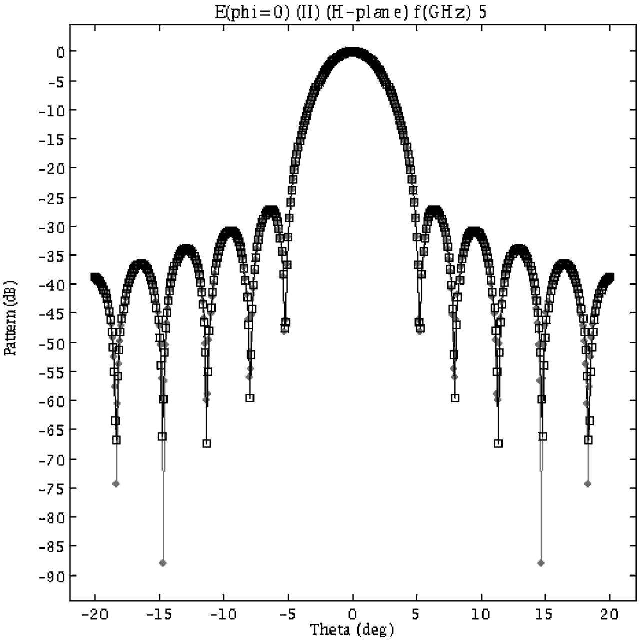

Fig. 6 The 5-GHz H-plane antenna pattern with no plume (♦) and the reference pattern (□).

The 5-GHz copolarization H-plane antenna pattern for this configuration, generated by the ray-tracing code with the thruster turned off, is shown in Fig. 6. No cross polarization is obtained. The E-plane pattern is identical. The pattern agrees with the analytical result given by Eq. (81), which is also plotted in Fig. 6.

The 5-GHz copolarization H-plane antenna pattern with the thruster turned on and $x_p = -0.8$ m is shown in Fig. 7. The plume has a significant impact. A beam squint of 0.4 deg occurs, with the main lobe bending away from the thruster. The main lobe has been attenuated about 1.5 dB. (This is not a real attenuation in terms of power absorption by the plasma. Rather, it is a redistribution of power into the side lobes.) The side lobes are not symmetric, with particular degradation of the first two side lobes for positive theta. No cross polarization within the computational accuracy is obtained.

The E-plane copolarization pattern is shown in Fig. 8. The side lobes have merged, degrading the sharp main lobe into a broad overall pattern. The cross polarization is less than −85 dB. (The larger cross polarization reported in Refs. 6 and 19 was due to imprecise evaluation of the torsion τ.)

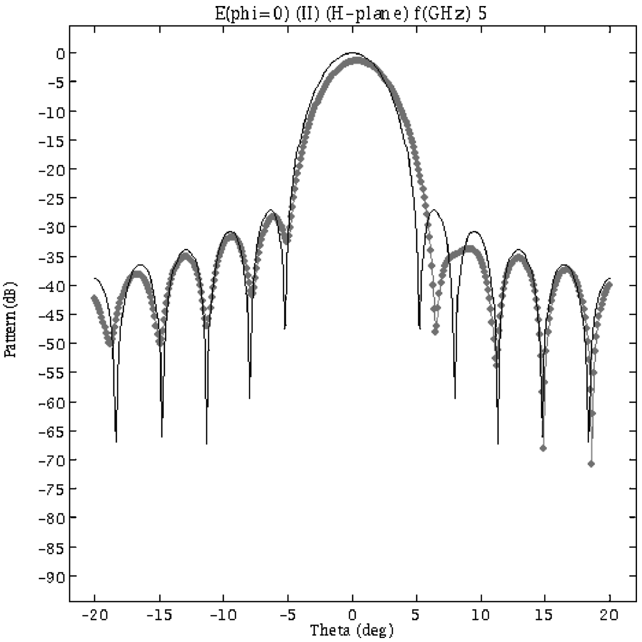

Fig. 7 The 5-GHz H-plane antenna pattern with plume on (♦) and $x_p = -0.8$ m; reference pattern also plotted.

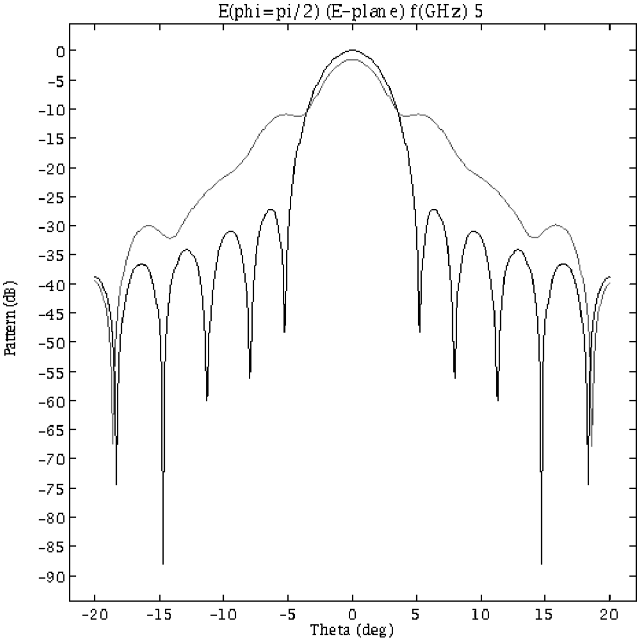

Fig. 8 The 5-GHz E-plane antenna patterns with plume on and $x_p = -0.8$ m (broad curve) and plume off.

A plot of the ray locations on the exit plane is shown in Fig. 9. Figure 9a is with the thruster turned off and Fig. 9b is with the thruster on and $x_p = -0.8$ m. The axes for these plots is referenced to the boresight of the antenna, as shown in Fig. 5. For each ray, a square is drawn at the location the ray intersects the exit plane. The area of the square is equal to the ray tube area at the exit plane (the square gives no information on the actual shape of a ray tube, which is not computed). Rays in Fig. 9a do not overlap and form a 1-m-diam circle because they simply propagate in the z direction from their launch point on the 1-m-diam reflector.

Figure 9b, with the thruster on, shows both deflection of rays and changes in the ray tube areas caused by the plasma. Rays are bent away from the plume (the refractive index of the plasma is less than unity, and rays bend toward regions of higher refractive index). This is particularly evident at negative exit-normal (EN) locations, which are closer to the plume. The rays are bent symmetrically in

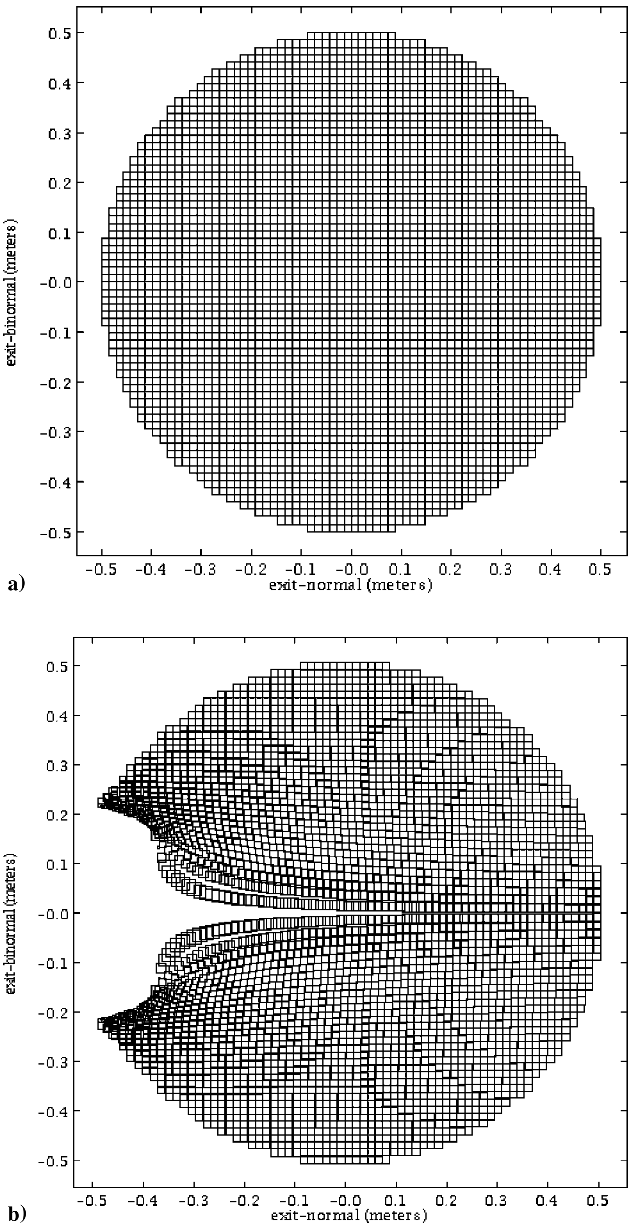

Fig. 9 Ray locations on the exit plane with a) thruster off and b) thruster on and $x_p = -0.8$ m.

the exit-binormal (EB) direction because the plume is symmetric in this direction. The plasma both focuses and defocuses ray tubes, as shown by the smaller and larger squares for rays that have traveled through denser plasma regions (reflecting divergence factors greater than one and less than one at the exit plane, respectively). Defocusing is evident for rays close to the EB axis in Fig. 9b, whereas focusing occurs for rays near $EN = -0.4$ m, $\mathrm{EB} = \pm 0.2$ m.

To study the thruster impact as a function of distance from the antenna, x_p was changed from -0.6 to -2.0 m in 0.2-m increments. The E-plane copolarization patterns for all of the thruster positions are shown in Fig. 10. The pattern with the plume turned off is also plotted (curve with the largest main lobe amplitude). From Fig. 10, the merging of the first side lobe into the main lobe is clearly evident. No cross polarization within the computational accuracy is obtained.

The attenuation of the main lobe is shown in Fig. 11. The attenuation at 5 GHz is less than 0.1 dB until the thruster is about 1.4 m from the reflector center (0.9 m from the reflector edge) and then rapidly increases. The main lobe attenuation at 10 GHz is about a factor of four lower at all positions, giving $1/\omega^2$ scaling. The width of the H-plane main lobe is relatively constant, increasing slightly for x_p greater than -1 m, as shown in Fig. 12. In Fig. 12, circles are 5-GHz data and squares are 10 GHz. The no plume widths are 9.0, 7.0, 4.4, and 3.4 deg for the curves from the top to the bottom of the graph.

The E-plane copolarization amplitudes are plotted as a function of thruster position x_p at $\theta = 5$ deg (5 GHz) and $\theta = 2.5$ deg (10 GHz) in Fig. 13. Circles are 5-GHz data, and squares are 10-GHz data. With no plume, the amplitude is -32 dB. These theta values are close to the no plume first null, as shown in Fig. 10 for 5 GHz. These amplitudes give a measure of side lobe degradation. The curves have similar shapes at both frequencies, with the amplitude about 5 dB lower at 10 GHz.

The studies just described were done on a 333-MHz Pentium II Personal Computer with 128-MB memory, running the Linux operating system. Each 5-GHz configuration (3640 rays) took about 1.5 h to run. Each 10-GHz case (14,108 rays) took about 5 h and 45 min to run. The web interface is described in the Appendix.

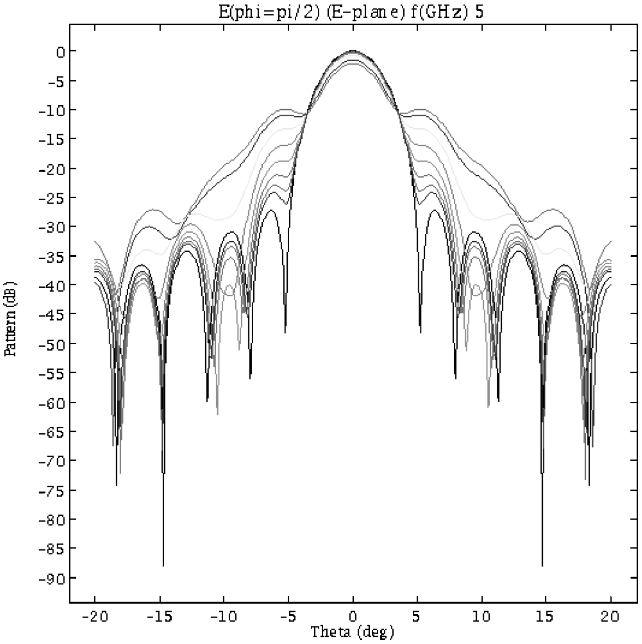

Fig. 10 E-plane antenna patterns for all thruster positions at 5 GHz.

Accuracy

The BeamServer code consists of ray tracing algorithms and a far-field pattern calculation from the exit plane. The pattern calculation can be verified by running the code with no plasma and comparing the pattern with the known analytical solution [Eq. (81)]. This agreement is line-on-line, as shown in the results section. With no plasma, the ray trajectories are straight lines, and agreement with the reference pattern does not check the ray calculations in an inhomogeneous medium. For this we replace the plasma with an inhomogeneous medium with known analytical ray solution, such as the Luneburg lens (see Ref. 20). BeamServer computation of the endpoint ray location, optical path length, and focal spot size for a 0.25-m-radius Luneburg lens is accurate to $\sim 10^{-5}$ m. In addition, we have studied the effect of changing the step size in the BeamServer calculations. These tests lead us to conclude that computations of the ray location, phase, electric field, and polarization at the exit plane have at least six significant figures of precision.

The GO approach provides another source of error. This includes sampling requirements and the GO approximation. Results presented in this paper use Nyquist sampling at the ray launch point (antenna). This has been found to be more than sufficient; the resulting antenna patterns do not change with increased sampling. The GO approach does not include diffraction. The use of GO in the free-space design of reflector antennas is well developed. Studies have been performed[21] that indicate that the best surface to perform aperture field integration in a GO scheme is on a surface that caps (or nearly caps) the reflector completely. Projecting the fields out on an aperture leads to errors in the antenna pattern because GO is inherently an approximation to the entire field.

For this work, the exit plane must be located away from the reflector surface because this is the region containing the inhomogeneous plasma medium. The study given in the results section has the exit plane located 1 m from the reflector. To evaluate the error, we have run the 5-GHz, $x_p = -0.8$ m configuration with varying exit plane locations. Changing the exit plane from 0.8 to 1.5 m changes the central lobe only slightly. The central lobe peak amplitude changes about 0.15 dB and shifts about 0.25 deg. The side lobes are more strongly affected. Side lobe positions shift as much as several degrees, and their amplitudes change by as much as 5 dB.

Results are also determined by the plume model. HTs have a considerable range of operation, unit-to-unit variation, and a more complex density structure than represented by our model. Finally, the aperture launch of rays presented here does not include the reflector

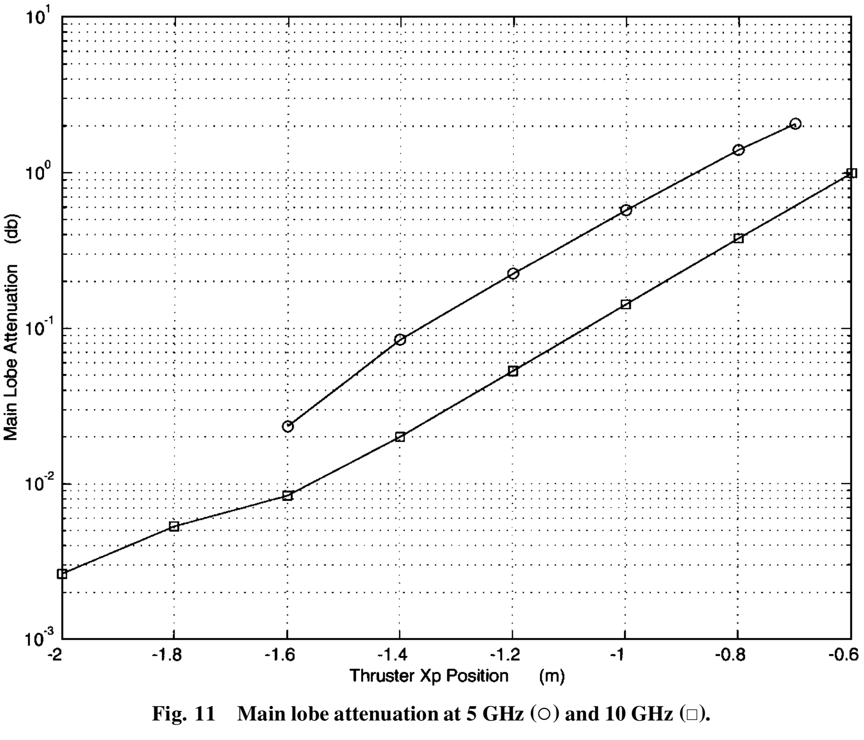

Fig. 11 Main lobe attenuation at 5 GHz (○) and 10 GHz (□).

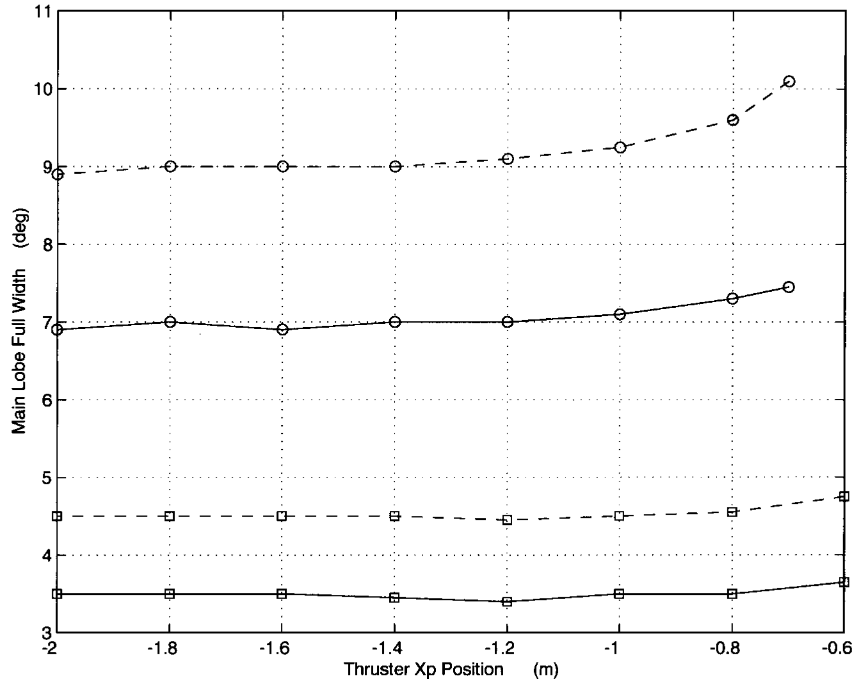

Fig. 12 H-plane main lobe full width at 10 dB (——) and 20 dB (- - -) down from the peak amplitude.

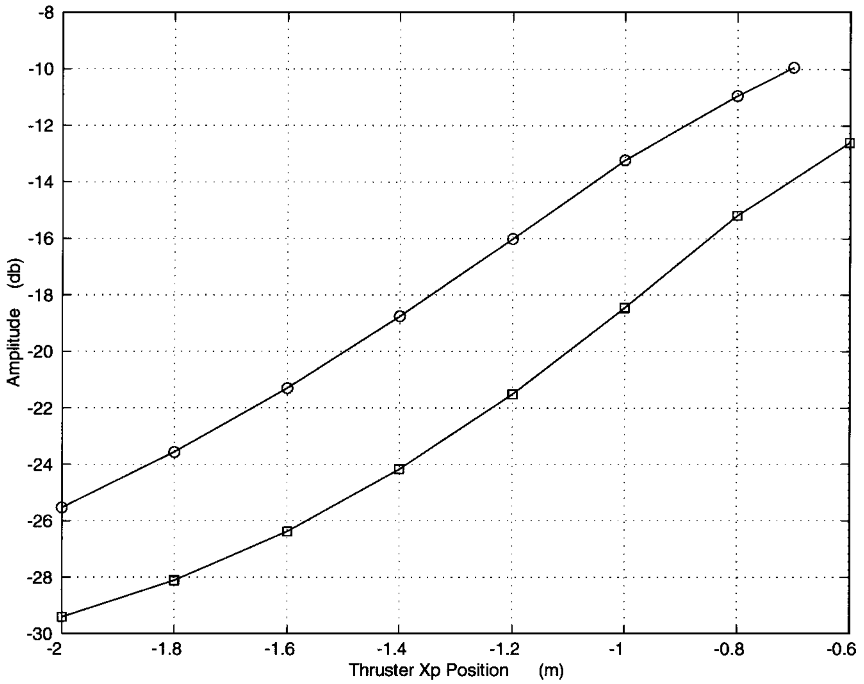

Fig. 13 E-plane copolarization amplitude showing off-axis power increase as the thruster is brought closer to the antenna beam.

feed. In general, the plasma thruster can interact with the signal beam twice, once from the reflector feed to the reflector and again as the beam propagates away from the reflector. Note that, although there are errors in the absolute antenna patterns, the relative changes in the antenna patterns occurring when the thruster position is scanned should be more accurate.

Conclusions

A sophisticated ray-tracing code has been developed to study the effect of a plasma plume on reflector antennas. The code allows arbitrary geometry and has a friendly web-based interface. Studies undertaken with the code quantify the major effects: main beam attenuation and squinting and side lobe degradation. Parametric studies, such as presented here, are useful in understanding the basic interaction and show that the degradation can be small with sufficient plume–antenna separation. Detailed analysis of proposed configurations should follow. Future enhancements to the code will include the feed (rather than starting rays at the reflector), other normalizations, shaped reflectors, and modulation.

Appendix: Web Interface

The user interface to the C++ code is a graphical user interface. This interface allows network operation, configuration setup by entering parameters in various boxes, and graphical display of results as requested. The system is set up using a client/server architecture. The BeamServer client is written in JAVA, and the server is C++ and JAVA. Communications uses the CORBA protocol.

The idea of a client/server program is that the program is divided into two parts. The client handles the user interface and can be executed on a number of machines on a network (usually the user's computer). The main computational kernal is located on a server machine that has significant computational resources. Both the client and server can run on the same machine if desired.

When the client is run, the first window that opens is the connect window. This window allows the client to connect to a running server or to start a new server. A list of the currently running servers is displayed by selecting connect under the file menu. A new box will open, allowing one to scroll through the list of currently running servers. One can generally connect and disconnect from a running server without causing the server to execute or lose its state.

Once connected to a running server, the main program control window opens. Buttons on this window will run the ray-tracing code, edit the configuration, or display results. Various plots may be made, including xy, contour, and three dimensional. Results such as the antenna patterns, ray trajectories, and quantities along a ray trajectory (such as the index of refraction) may be displayed.

Data may be saved in files for later analysis. State files may also be generated of a particular configuration. These state files can be loaded back into the program, reestablishing a configuration of interest. A command file can be set up to run a number of cases, such as described in the results section of this paper. This independent operation is useful because the program typically requires several hours to run each configuration.

Acknowledgments

This work is supported by Lockheed Martin Corporation under Purchase Order AUCEC6002F and by the Texas Higher Education Coordinating Board under Grant ATP-371. The authors would like to thank H. Ling for many useful discussions.

References

[1] Gulczinski, F. S., III, Gallimore, A. D., Carlson, D. O., and Gilchrist, B. E., "Impact of Anode Layer Thruster Plumes on Satellite Communications," AIAA Paper 97-3067, July 1997.

[2] Ohler, S. G., Gilchrist, B. E., and Gallimore, A. D., "Electromagnetic Signal Modification in a Localized High-Speed Plasma Flow: Simulations and Experimental Validation of a Stationary Plasma Thruster," *IEEE Transactions on Plasma Science,* Vol. 27, No. 2, 1999, pp. 587–594.

[3] Berthou, C., and Pogaricloff, D., "SPT100 Plasma Jet Effects on Geostationary Satellite Communications," International Electric Propulsion Conf., IEPC Paper 99-074, 1999.

[4] Oh, D., and Hastings, D.,"Three Dimensional PIC-DSMC Simulations of Hall Thruster Plumes and Analysis for Realistic Spacecraft Configurations," AIAA Paper 96-3299, July 1996.

[5] Dickens, J. C., Mankowski, J., Kristiansen, M., and O'Hair, E., "Impact of Hall Thrusters on Communication System Phase Noise," AIAA Paper 95-2929, July 1995.

[6] Ling, H., Kim, H., Hallock, G. A., Birkner, B. W., and Zaman, A. J. M., "Effect of an Arcjet Plume on Satellite Reflector Performance," *IEEE Transactions on Antennas and Propagation,* Vol. 39, No. 9, 1991, pp. 1412–1420.

[7] Carney, L. M., "Evaluation of the Communications Impact of a Low Power Arcjet Thruster," AIAA Paper 88-3105, July 1988.

[8] Birkner, B. W., Hallock, G. A., Kim, H., and Ling, H., "Arcjet Plasma Plume Effect on a Microwave Reflector Antenna," *Review of Scientific Instruments,* Vol. 61, No. 10, 1990, pp. 2978–2980.

[9] Ohler, S., Gilchrist, B. E., and Gallimore, A., "Microwave Plume Measurements of a Closed Drift Hall Thruster," *Journal of Propulsion and Power,* Vol. 14, No. 6, 1998, pp. 1016–1021.

[10] Ling, H., Hallock, G. A., Kim, H., and Birkner, B. W., "Near Field Interaction of Microwave Signals with a Bounded Plasma Plume," Annual Rept., Grant NCC3-127, Dept. of Electrical and Computer Engineering, Univ. of Texas, Austin, TX, Jan. 1990.

[11] Stavroudis, O. N., *The Optics of Rays, Wavefronts, and Caustics*, 1st ed., Academic Press, New York, 1972, pp. 32, 33, 142, 143.

[12] Press, W. H., Flannery, B. P., Teukolsky, S. A., and Vetterling, W. T., *Numerical Recipes*, 1st ed., Cambridge Univ. Press, Cambridge, England, U.K., 1986, pp. 563–568.

[13] Bremmer, H., and Lee, S. W., "Propagation of a Geometrical Optics Field in an Isotropic Inhomogeneous Medium," *Radio Science,* Vol. 19, No. 1, 1984, pp. 243–257.

[14] Tuma, J. J., *Engineering Mathematics Handbook*, 3rd ed., McGraw–Hill, New York, 1987, p. 439.

[15] Rahmat-Samii, Y., "Reflector Antennas," *Antenna Handbook,* edited by Y. T. Lo and S. Lee, Vol. 2, Van Nostrand Reinhold, New York, 1993, pp. 15.15–15.16.

[16] Born, M., and Wolf, E., *Principles of Optics*, 7th ed., Cambridge Univ. Press, New York, 1999, pp. 125–127.

[17] Lee, S. W., Ling, H., and Chou, R., "Ray-Tube Integration in Shooting and Bouncing Ray Method," *Microwave and Optical Technology Letters,* Vol. 1, No. 8, 1988, pp. 286–289.

[18] Ling, H., Chou, R., and Lee, S., "Shooting and Bouncing Rays: Calculating the RCS of an Arbitrarily Shaped Cavity," *IEEE Transactions on Antennas and Propagation,* Vol. 37, No. 2, 1989, pp. 194–205.

[19] Hallock, G. A., Wiley, J. C., Khanna, A., Spencer, E. A., Meyer, J. W., and Loane, J. T., "Impact Analysis of Hall Thrusters on Satellite Communication," AIAA Paper 2000-3519, July 2000.

[20] Chan, A. K., "Optical Wave Propagation," *Handbook of Microwave and Optical Components,* edited by K. Chang, 1st ed., Vol. 3, Wiley-Interscience, New York, 1990, p. 24.

[21] Yaghjian, A. D., "Equivalence of Surface Current and Aperture Field Integrations for Reflector Antennas," *IEEE Transactions on Antennas and Propagation,* Vol. AP-32, No. 12, 1984, pp. 1355–1358.

A. C. Tribble
Associate Editor